Gaussian beam deconvolution in optical coherence tomography

Tyler S. Ralston[a,b], Dan Marks[a,b], Farzad Kamalabadi[b], and Stephen A. Boppart[a,b,c,*]

[a]Beckman Institute for Advanced Science and Technology
University of Illinois Urbana-Champaign 405 N. Mathews Ave. Urbana, IL 61801
[b]Department of Electrical and Computer Engineering
University of Illinois Urbana-Champaign, 1406 W. Green St. Urbana, IL 61801
[c]Bioengineering Program, College of Medicine
University of Illinois Urbana-Champaign

ABSTRACT

Optical coherence tomography (OCT) is an emerging, high-resolution near-infrared imaging and microscopy technique. The axial and transverse resolutions in OCT can each be analyzed independently, with the axial resolution inversely proportional to the spectral bandwidth of the optical source and the transverse resolution defined by standard Gaussian beam optics. While high numerical-aperture objectives are preferred to improve the transverse resolution, the reduced confocal parameter limits the depth-ranging capabilities of OCT and more complex en face imaging with focus tracking must be employed. We present a method for increasing the apparent transverse resolution in OCT outside of the confocal parameter using Gaussian beam deconvolution of adjacent axial scans, and thereby reducing the limitations associated with the hourglass profile of a tightly focused Gaussian beam. Specifically, our method determines how measurements depend on the object when blurred with a Gaussian beam, and subsequently finds an estimate of the original object. Possible reconstruction estimates are explored and evaluated using a variety of regularization techniques as well as estimation maximization algorithms. Numerical simulations demonstrate effectiveness of each technique. When applied to experimentally-acquired OCT data, the use of these algorithms can improve the apparent transverse resolution outside of the confocal parameter, extending the comparable confocal parameter range along the axial direction. These results are likely to further improve the high-resolution cross-sectional imaging capabilities of OCT.

Keywords: Optical coherence tomography, Deconvolution, Gaussian beam, Transverse resolution, Focusing, Richardson-Lucy.

INTRODUCTION

Optical coherence tomography (OCT) is an emerging, near-infrared imaging and microscopy method capable of micrometer-scale resolutions in biological specimens[1-3]. In an OCT system, axial resolution is inversely proportional to the spectral bandwidth of the optical source, which is dependent on the optical coherence. The intensity versus the difference in reference and sample path lengths with respect to time is called an *interferogram*; it is the cross-correlation signal. The interferogram is a real signal, thus it is composed of positive and negative frequencies. The interferogram can be used to generate a complex analytic signal composed of only positive frequencies. Doppler OCT and structural OCT images are generated using the phase and magnitude information of the complex analytic signal[4-6]. The complex analytic signal is most relevant when deciding the feasibility of each algorithm presented in the following sections. Specifically, some algorithms have positivity constraints[7,8], that do not apply to OCT refractive index reconstruction, but still may be useful under an assumption of point-like scatterers.

Typically, assembling transverse-aligned, adjacent axial scans generates a two-dimensional, cross-sectional OCT image[2,3]. Namely, the beam is assumed to be perfectly collimated at every point in the sample. However, in Gaussian optics, the geometry of the beam profile exhibits an hourglass shape after passing through a lens, as illustrated in fig. 1. This profile assumes a direction of propagation incident perpendicular to the lens. The transverse resolution is not constant, but has a dependence on the depth and the focal region of the lens. Furthermore, lenses with a higher

* For correspondence with Dr. Stephen A. Boppart email: boppart@uiuc.edu phone: (217) 244-7479

Three-Dimensional and Multidimensional Microscopy: Image Acquisition and Processing XII, edited by José-Angel Conchello, Carol J. Cogswell, Tony Wilson, Proc. of SPIE Vol. 5701 (SPIE, Bellingham, WA, 2005) · 1605-7422/05/$15 · doi: 10.1117/12.590443

numerical aperture (NA) are able to focus a beam to a smaller spot size but produce a more pronounced hourglass shape. Hence, high NA lenses are typically used for optical sectioning in planes parallel (*en face*) to the surface of the specimen such as in confocal or multiphoton microscopy[9]. Lenses with a lower numerical aperture are typically preferred for OCT, where a relatively uniform transverse resolution over the entire axial (depth) scan is desired. Typically when choosing a lens for OCT, the confocal parameter (distance about the focus where the beam width is relatively uniform) is chosen to closely match the depth of imaging penetration in a particular tissue type.

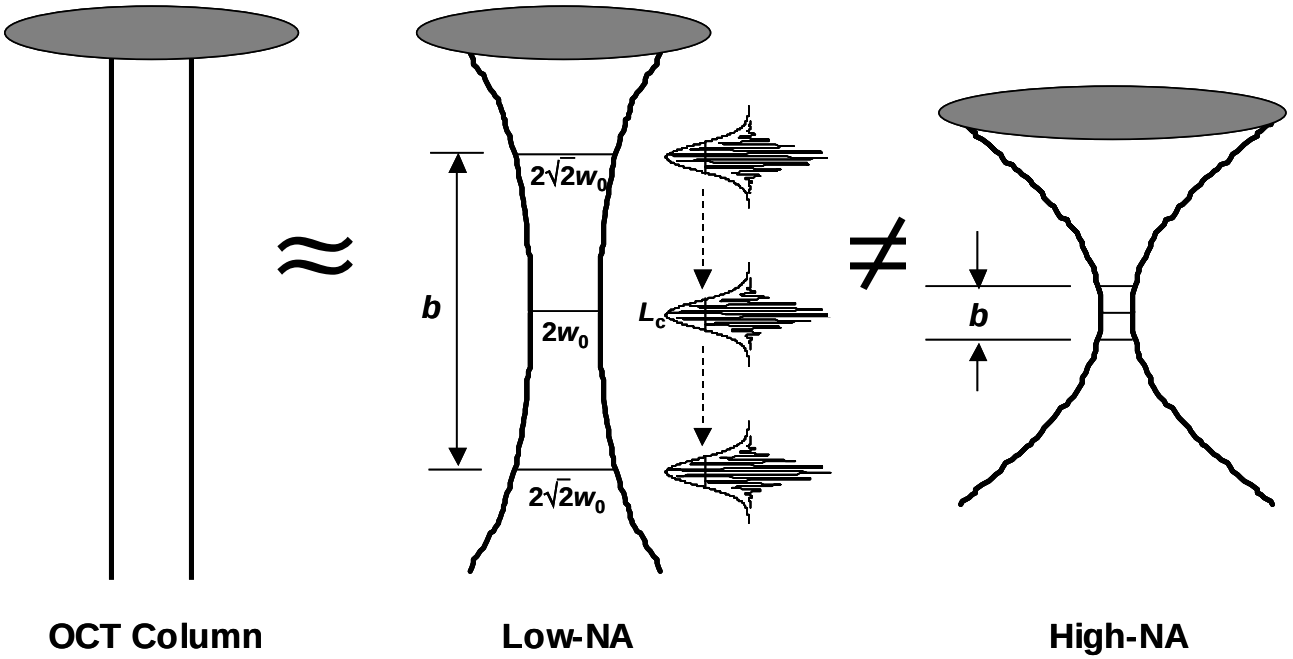

Fig. 1. The geometry of a Gaussian beam for low and high numerical aperture (NA) lenses. These geometries are contrasted with the assumption of a collimated axial OCT scan. b is the confocal parameter, w_o is the beam radius at the focus, and L_c is the coherence length of the source.

The transverse resolution R_T is approximately the diameter of the spot size, $2w_o$, which is the width of the incident beam on the sample where the edges are determined by a marked decrease in intensity, and is approximated by

$$R_T \approx 2w_o \approx 2.44\frac{f\lambda_o}{D}\ , \tag{1}$$

where f is the focal length of the lens, D is the beam diameter incident on the objective lens, and λ_o is the central wavelength. The confocal parameter can be defined as

$$b = \frac{\pi R_T^{\ 2}}{2\lambda_o}. \tag{2}$$

Equation (2) indicates that the size of the confocal region decreases as the square of the transverse resolution decreases. Transverse resolution is significantly reduced outside of the confocal region, thus blurring features of the specimen. In OCT, the focusing Gaussian beam profile remains fixed, while varying the reference arm pathlength scans the depth at which backscattered signal is detected. In OCT images, if a high NA objective is used and the depth scan length exceeds the dimension of the confocal region, then the loss of transverse resolution will be evident in the image and features located outside of the confocal region will appear blurred. Our goal for this research is to digitally reduce the transverse blurring outside of the confocal region by using deconvolution techniques. The solution will be to determine how OCT measurements depend on an object that is blurred with a Gaussian beam, and then find a suitable estimate of the deblurred signal.

A multitude of deconvolution algorithms has been developed for estimating a genuine signal based on idealizations of physical properties. For instance, the astronomy community has developed several algorithms, which

have proven to be paramount for extracting relevant stellar information[10]. Furthermore, optical microscopy has benefited from use of these restoration techniques, which solve problems such as out-of-focus flare in fluorescence imaging[11]. Several deconvolution algorithms have been implemented in OCT to correct for axial blurring[12-14]. These algorithms correct either the effect of the laser spectrum or the dispersion induced by the optical system and the specimen. Experimental setups have utilized additional optical hardware such as adaptive optics or axicon lenses to increase the transverse resolution over large depths in the specimen[15,16]. Dynamic focusing techniques have been implemented for OCT and optical coherence microscopy to generate images with high transverse resolutions over relatively large depths, which can be useful for *en face* imaging[2,17]. Although these methods are feasible, each requires specific hardware modifications that may be expensive or difficult to control in the OCT system setup. One algorithm for generating OCT images with high transverse resolution over large apparent depth scans involves composite (C-mode) imaging[18], and is analogous to one used in ultrasound imaging. This algorithm involves the acquisition of multiple OCT images, with the beam focus placed at incrementally increasing depths within the specimen. From each image, data located within the short confocal region is segmented out and subsequently assembled to produce a single composite image. A significant advantage of the transverse deconvolution algorithm presented here is the reduction of the transverse blurring and the apparent improvement in transverse resolution inside and outside of the confocal region without the addition of new optical hardware or the need to acquire multiple images of the same specimen.

The main objective of this study is to investigate a set of algorithms for improving the transverse resolution of OCT by deconvolving the Gaussian beam blurring caused by a lens. The next section demonstrates a general approach to modeling the physical parameters that characterize the lens. Then, a number of solutions to remove the effect of the Gaussian beam blur are introduced. Simulations for each of these solutions are used to assess algorithm performance. Finally, the algorithms are applied to experimentally-acquired OCT images to further characterize the Gaussian beam problem.

A more uniform resolution throughout an image can impact the way an object is categorized. For example, a biological specimen with pre-cancerous cellular changes may go unnoticed if it lies in an imaging region where the blurring occurs[19,20], and a non-uniform resolution could result in a misdiagnosis[21]. Finally, there is the potential for reducing data acquisition time since a higher percentage of the OCT image may be more clinically useful.

MODELS AND METHODS

It is necessary to create an accurate mathematical model of the transverse beam dynamics in the OCT system to characterize the transverse resolution. Specifically, the Gaussian beam profile of the lens characterizes the depth-dependent lateral resolution. A Gaussian beam can be represented by the following equation:

$$G(\vec{r}) = A_0 \frac{W_0}{W(z)} \exp\left(-\frac{\rho^2}{W^2(z)}\right) \exp\left(-jk(\omega)z - jk(\omega)\frac{\rho^2}{2R(z)} + j\zeta(z)\right), \tag{3}$$

where the depth dependent beam waist size is given by

$$W(z) = W_0 \left[1 + \left(\frac{z}{z_0}\right)^2\right]^{1/2}, \tag{4}$$

the radius in Cartesian coordinates is given by

$$\rho = \sqrt{x^2 + y^2}, \tag{5}$$

the radius of curvature of the wavefront is given by

$$R(z) = z\left(1 + \left(\frac{z_0}{z}\right)^2\right), \tag{6}$$

the Guoy phase shift is

$$\zeta(z) = \tan^{-1}\left(\frac{z}{z_0}\right), \tag{7}$$

and the wave number (neglecting dispersion) is given by

$$k(\omega) = k_0 + \frac{\omega - \omega_0}{v_g}, \tag{8}$$

where v_g is the group velocity (envelope speed), k_0 is a constant wave number, ω_0 is a constant frequency, ω is the frequency of the light, A_0 is a constant amplitude, W_0 is the waist radius, x and y are the transverse coordinates, and z is the axial coordinate where $z=z_0$ at the boundary of the confocal region[22]. The wavefronts are approximately planar at the beam waist, but gradually curve at distances away from the waist (outside of the confocal region). The wavefront emitted from a scattering object in the Gaussian beam has a curvature dependent on the phase term, $-jk\frac{\rho^2}{2R(z)}$. The Gaussian wavefront has spherical constant-time surfaces that in this work are approximated as planes. Fig. 2 shows the cross-section of curved wavefronts in gray and the planar wavefronts as dashed lines. The Gaussian beam equation for planar wavefronts is

$$G(x, y, z) = \frac{W_0}{W(z)} \exp\left(-\frac{x^2 + y^2}{W^2(z)}\right) \exp\left(-j\left(k_0 + \frac{\omega - \omega_0}{v_g}\right) z\right). \tag{9}$$

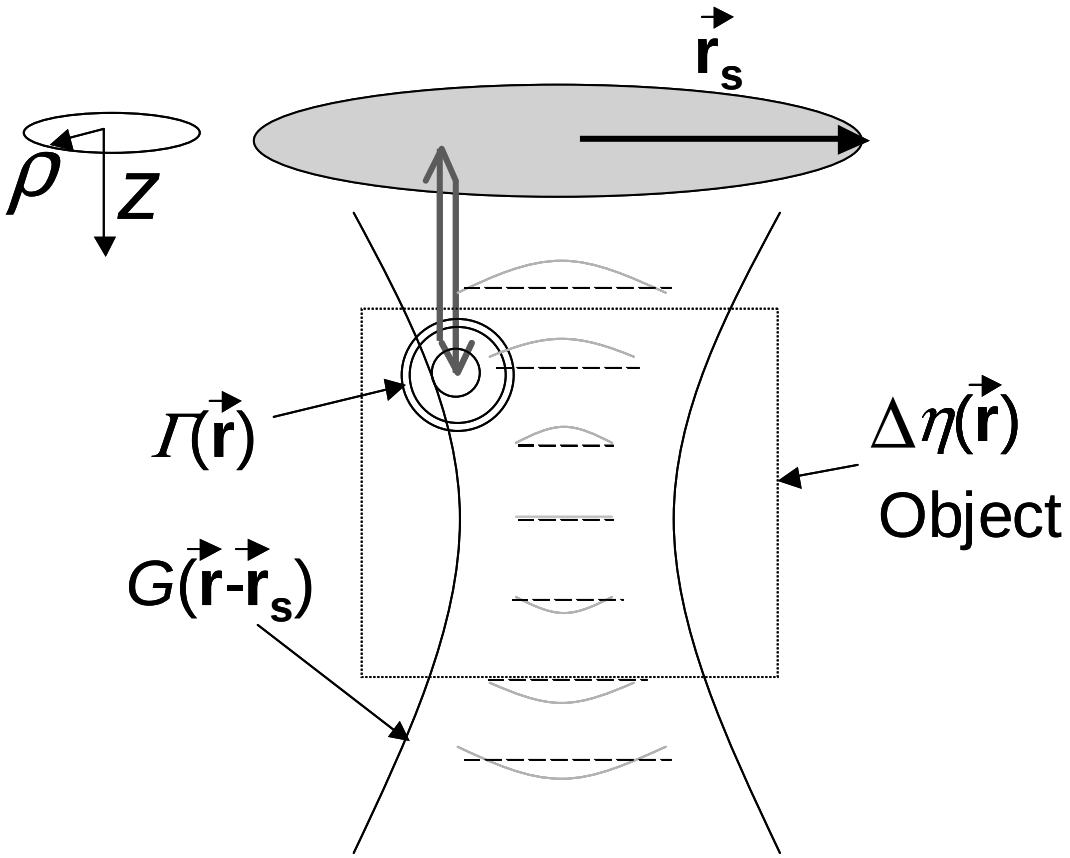

Fig. 2. Gaussian beam wavefronts from nonlinear exponential quantities (solid gray) and an approximation with the quantities removed (dashed), $\vec{r}_s$ is the vector from the center of the lens to a scatterer, $G(\vec{r})$ is the Gaussian envelope, $\Gamma(\vec{r})$ is the Green's function, and $\Delta\eta(\vec{r})$ is the index of refraction change in the imaged medium. Red arrows represent the first Born approximation (single backscatter).

Fig. 2 also diagrams the first Born approximation, usually sufficient in OCT, as applied to the Gaussian beam deconvolution problem. The Green's function $\Gamma(\vec{r})$ represents the reflection due to a change in index in the imaged object, $\Delta\eta(\vec{r})$. The Gaussian beam profile is $G(\vec{r}-\vec{r}_s)$, where $\vec{r}_s$ is the distance from the center of the lens. Thus, a first Born (single scattering) approximation of the reflection is given by

$$R(\vec{r}) = \Gamma(\vec{r}) * \left(\Delta\eta(\vec{r}) \cdot G(\vec{r}\text{-}\vec{r}_s)\right), \tag{10}$$

where * denotes three-dimensional spatial convolution.

A single axial scan of OCT data can be formulated as the projection of reflected light returning into the lens from the Gaussian beam,

$$\tilde{S}(r_s, \omega) = \int G(\vec{r}-\vec{r}_s)\left[\Gamma(\vec{r}) * \left(\Delta\eta(\vec{r}) G(\vec{r}-\vec{r}_s)\right)\right] d\vec{r}\ . \tag{11}$$

When the spherical waves from the Gaussian beam are scattered off of the object, they are matched to the mode re-entering the fiber. Thus, in the paraxial zone, the field collected by the fiber can be approximated by:

$$\tilde{S}(\vec{r}_s, \omega) = \int \Delta\eta(\vec{r})\left[G(\vec{r}-\vec{r}_s)\right]^2 dr\ . \tag{12}$$

Next, we can formulate the axial scan data as a function of time and space by integrating over the frequencies present in the laser spectrum $I(\omega)$,

$$\tilde{S}(x_s, y_s, t) = \int \tilde{S}(x_s, y_s, \omega) I(\omega) e^{-j\omega t} d\omega\ . \tag{13}$$

Equation (13) can be rewritten using (9) and (12) to get

$$\tilde{S}(x_s, y_s, t) = \int \left(\frac{W_0}{W(z)}\right)^2 \exp\left(-2j\left(k_0 + \frac{\omega_0}{v_g}\right)z\right) I\left(t - \frac{2z}{v_g}\right) \left[\int\int \Delta\eta(\vec{r}) \exp\left(-2\frac{\left((x-x_s)^2 + (y-y_s)^2\right)}{W^2(z)}\right) dxdy\right] dz\ , \tag{14}$$

where $I\left(t - \frac{2z}{v_g}\right)$ produces coherence gating, the quantity in square brackets represents a separable Gaussian convolution kernel having a depth-dependent standard deviation, $W(z)$, and the remaining terms represent a depth-dependent magnitude and phase. Next, we can estimate a *y*-blurred version of the object for an axial scan, $\tilde{S}(x_s, t)$ since kernel is separable. The bracketed quantity in (14) can be rewritten as

$$\int\left[\int \Delta\eta(x_s, y_s, z) \exp\left(-2\frac{(y-y_s)^2}{W^2(z)}\right) dy\right] \exp\left(-2\frac{(x-x_s)^2}{W^2(z)}\right) dx\ , \tag{15}$$

where the new bracketed term is a *y*-blurred version of the object and can be denoted by $\Delta\eta'(x_s, z)$. Therefore, by applying a deconvolution algorithm to each of the approximated Gaussian kernels in the *x* direction, the object can be reconstructed with blurring in only the *y* direction.

Since this design models noise, there will be a need for a regularized solution. The truncated SVD (TSVD) is used to provide a regularized solution,

$$x_{\text{TSVD}} = \sum_{i=1}^{k} \frac{u_i'^H y}{\sigma_i'} v_i'\ , \tag{16}$$

where *k* is determined by a regularization parameter, α, which is a corresponding threshold such that all $\sigma_i > \alpha$ are retained[23,24]. This method is chosen because it reduces the emphasis on smaller singular values in the minimum norm solution, which are more correlated to the noise.

Tikhonov regularization is also used,

$$x_{\text{Tikh}} = (A^H A + \lambda L^H L)^{-1} A^H y\ , \tag{17}$$

where λ is a regularization parameter, which can be estimated to be half the noise variance for a reasonable solution when L is the identity matrix[25,26]. Tikhonov regularization offers a method for compromising between the size of the residual norm and the side constraint, λ.

An iterative deconvolution scheme, known as Richardson-Lucy, converges to the maximum likelihood solution for Poisson statistical data, which is appropriate in some cases for modeling optical data that has shot noise, a result of counting statistics[27]. The algorithm is implemented in the following manner:

$$\hat{x}_{n+1,i} = \hat{x}_{n,i} \sum_j \frac{h_{j-i+1} y_j}{\sum_k h_{j-k+1} \hat{x}_{n,k}}, \tag{18}$$

where h_n is the point-spread function (PSF), in this case the Gaussian blurring kernel[7,8]. This method forces the restored image to be positive for each iteration.

SIMULATIONS

The simulations of the OCT system follow a method developed by Marks, et al.[12]. To create simulation OCT fringes for a set of point (delta) scatterers, (reflections from sub-resolution-sized particles), four parameters must be taken into account. First, the point scatterers must have random phase so as to model random positions of particles situated within a coherence volume. Second, the system must have bandwidth support, which is limited by the laser spectrum. The bandwidth of our system is 100nm and is centered at 820nm. Third, the lens must create a Gaussian beam depth-dependent blur. Our lens focal length f is 5mm, spot size $2w_0$ is 5μm, confocal parameter b is 48μm, and diameter of beam on the lens D is 2mm. Fourth, the system noise can be approximated with Gaussian white noise.

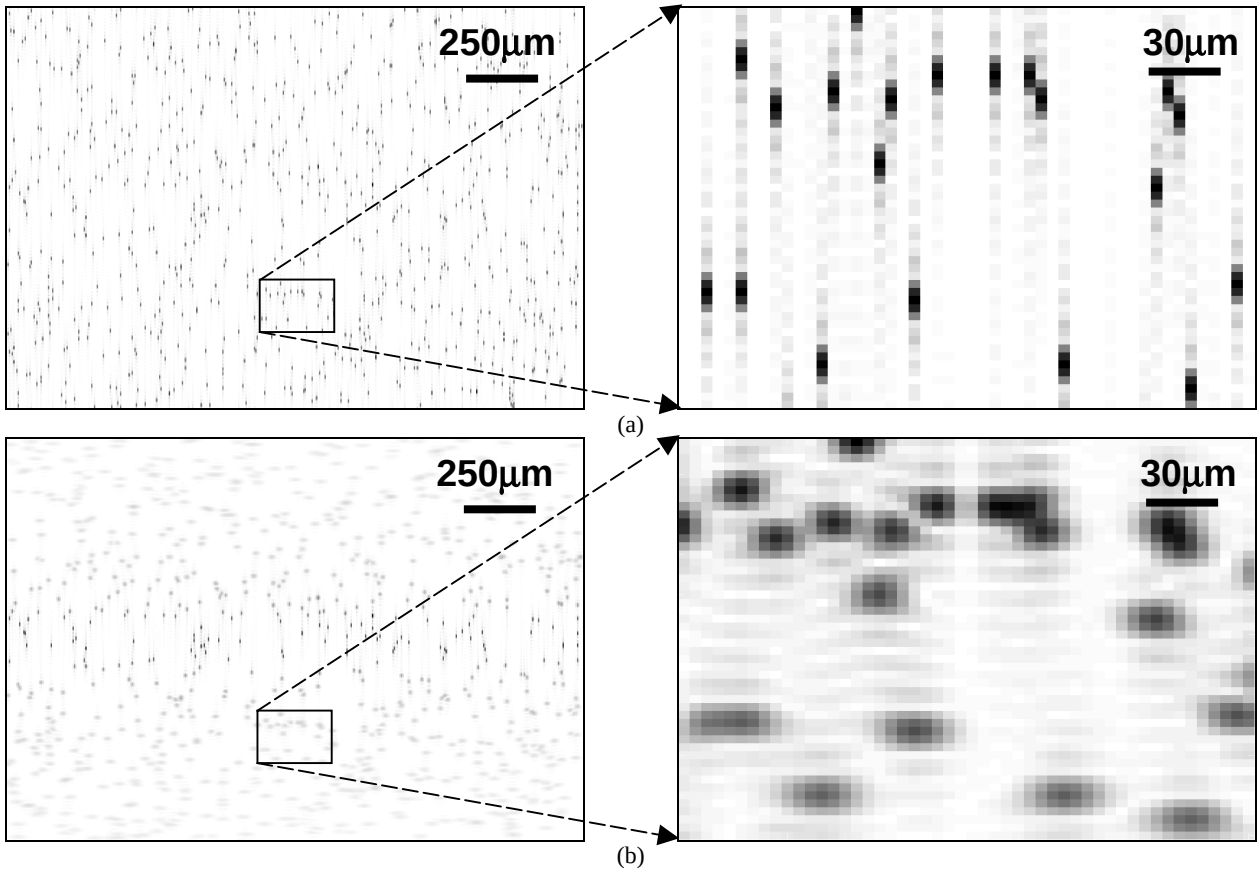

Fig. 3. Simulated OCT image of oversampled point scatterers. (a) Before a Gaussian beam blur (left) and zoom on scatterers (right), when parameters 1 and 2 are satisfied. (b) After a Gaussian beam blur (left) and zoom on scatterers (right), with SNR = 35 dB, and when parameters 3 and 4 are satisfied.

The effects of the first two parameters can be seen in fig. 3(a) and represent our deblurred and denoised image where delta scatterers are oversampled in the axial direction. The methodology for this testing is to characterize the resilience of the algorithm. Testing algorithms with a SNR of 35 dB serves to evaluate the algorithm performance and determine useful regularization parameters. The resulting image after addition of Gaussian blurring and white noise is seen in fig. 3(b). The simulated figures have every scatterer at the same position for direct comparison.

The minimum norm solution with Tikhonov regularization can be compared using both the magnitude and complex analytic fringe data. Several values for the regularization parameter were explored, but $\lambda = 0.02$ optimally balanced the seminorm with the residual norm when $L = I$.[28] Fig. 4(a) shows the reconstruction based on only the magnitude data. Reconstruction artifacts such as ringing are somewhat apparent in this image, while the reconstruction with the complex analytic signal has less ringing artifacts, as seen in fig. 4(b).

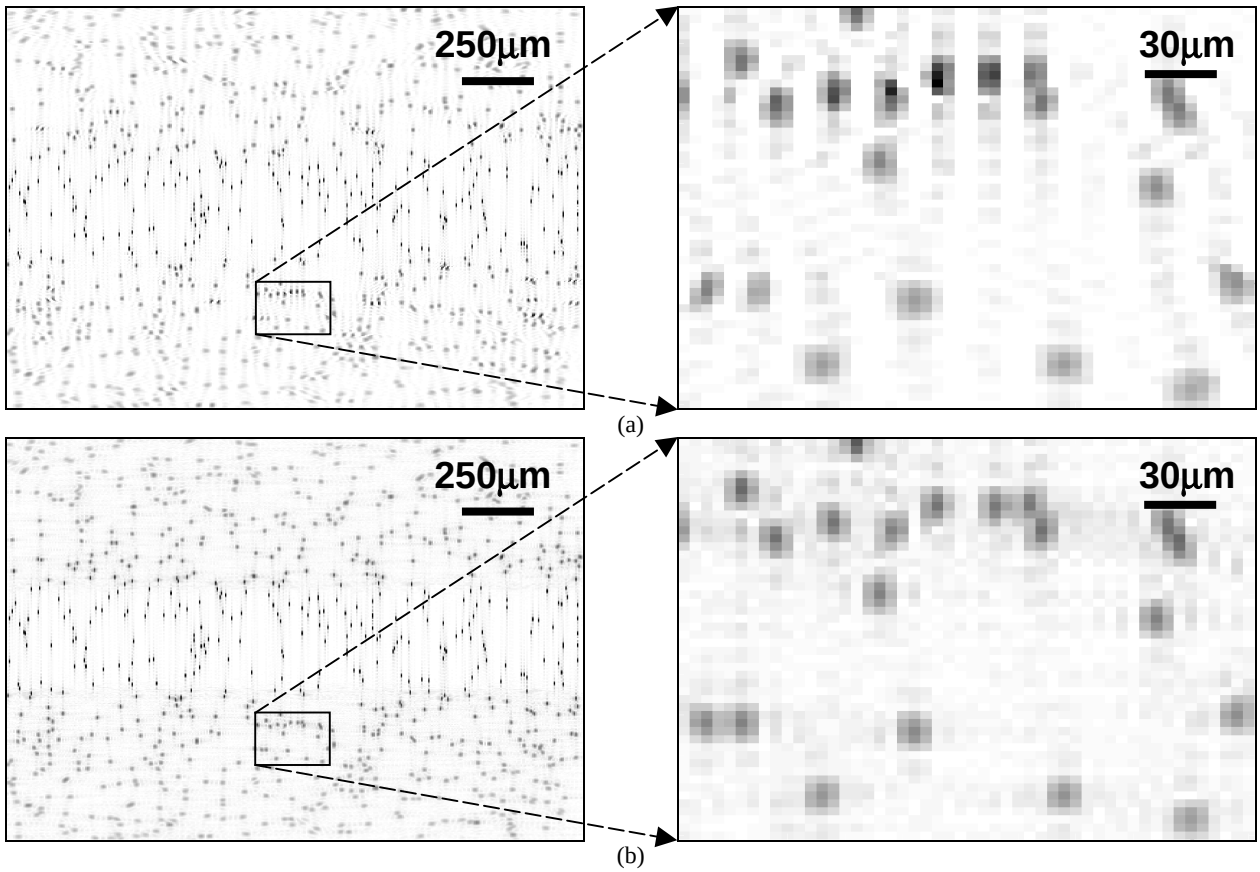

Fig. 4. Tikhonov regularization, $\lambda = 0.02$, SNR = 35 dB, using (a) magnitude signal (some ringing artifacts), and (b) complex analytic signal (minimal ringing).

The pseudo inverse with TSVD regularization is used to generate the minimum norm solution using both the magnitude and complex analytic fringe data. Several values for the regularization parameter were explored, but α = 0.01 optimally balanced the noise with the reconstruction (verified with the Picard condition)[28]. Fig. 5(a) shows the reconstruction based on only the magnitude data. Reconstruction artifacts such as ringing are quite apparent in this image, while the reconstruction with the complex analytic signal has minimal ringing artifacts, as seen in fig. 5(b).

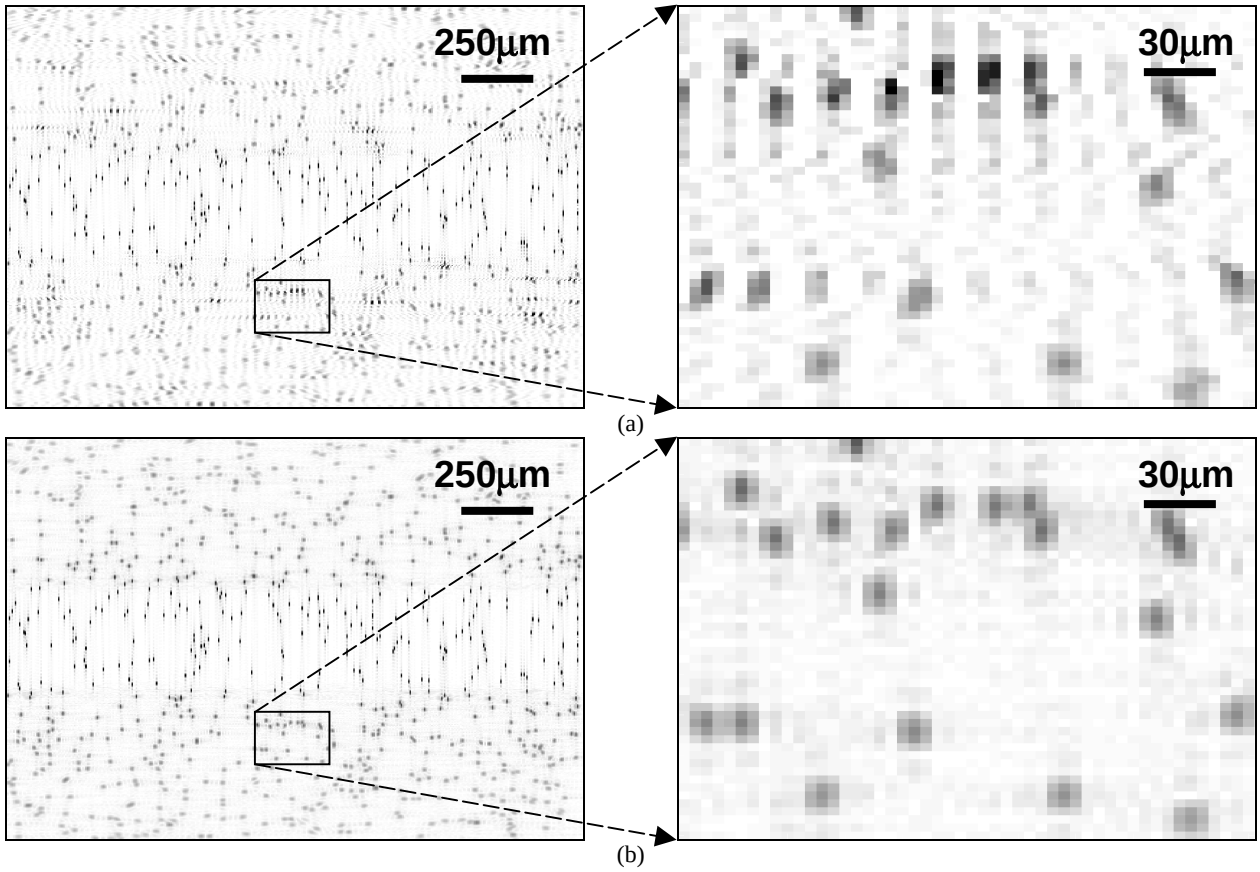

Fig. 5. Truncated singular value decomposition, α = 0.01, SNR = 35 dB, using (a) magnitude signal (ringing artifacts), and (b) complex analytic signal (minimal ringing).

Implementation of the Richardson-Lucy algorithm shows improvement in blurry regions of the image with increasing number of iterations. The Richardson-Lucy algorithm uses only the magnitude fringe data and has a positivity constraint for each iteration. Fig. 6(a) shows the magnitude data reconstruction for a single iteration of the Richardson-Lucy algorithm. Comparatively, since Gaussian beam blurring is a physical parameter, a number of iterations can be associated with each focal depth in the lens. Fig. 6(b) shows the magnitude for a dynamically-iterative reconstruction where the number of iterations is depth dependent. Specifically, the iterations increase proportional to the size of the Gaussian blurring kernel from 1 to 21. Some authors have addressed the optimality criterion for selecting parameters for algorithms like the Richardson-Lucy, which may lead to image convergence[29].

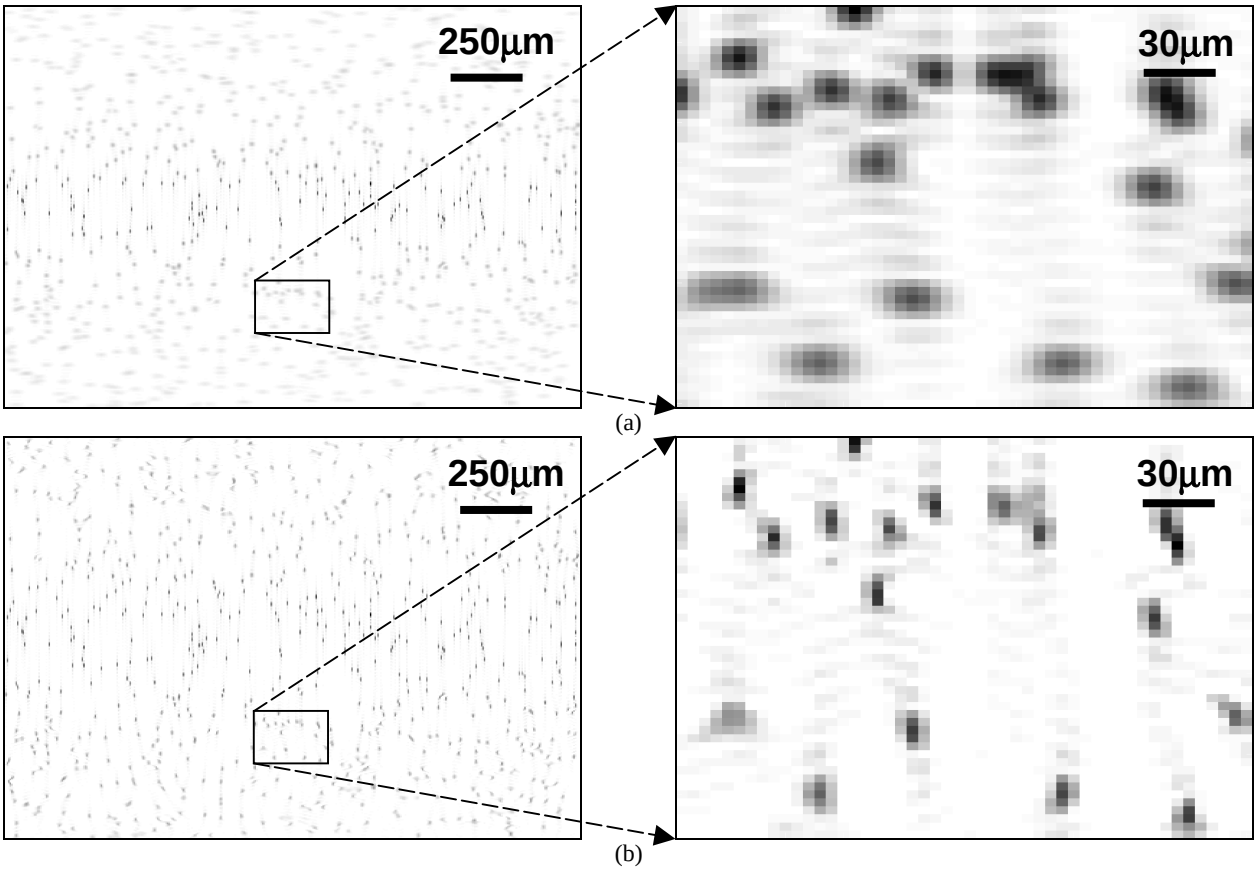

Fig. 6. Richardson-Lucy reconstruction using magnitude data, SNR = 35 dB, for (a) one iteration, and for (b) depth-dynamic iterations (1 to 21 linearly spaced from focus to image edge).

EXPERIMENTAL DATA

A tissue phantom was designed to test the point-spread function of our experimental setup. To design an appropriate tissue phantom, it is desirable to include individual scatterers on the size order of cellular structures and near our resolution limit. A solution of 4.0 grams of polydimethylsiloxane (PDMS) was mixed with 7 mg of Magnetite (Fe_3O_4), each having an average diameter of 1.9 μm. These microparticles act as point scatterers in OCT, thus providing a physical embodiment of our simulated experiment. Furthermore, these microparticles are used to simulate individual cells/nuclei in engineered tissues[30]. Images were taken at an axial scan rate of 25 Hz, with a 20 mm focal length lens, a system bandwidth of 100 nm full-width at half-maximum, a center wavelength of 800nm, and 15.6 mW of power incident on the sample. The calculated axial resolution is 3 μm, the transverse resolution was 15 μm, and the confocal region was 430 μm. Fig. 7 shows the original and Richardson-Lucy corrected images. The final deblurred region can be estimated by measuring the distance of the resolved points outside of the confocal region. The criteria for determining a resolved point is that the energy compaction of particles outside of the confocal region in the new image is equivalent to the energy compaction of particles on the edge of the confocal region in the original image. Based on this image data, the deblurred region extended over 500 μm above and below the confocal region, or a total distance of approximately 1.43 mm.

A second experiment was conducted by acquiring OCT image data from an *in vivo Xenopus laevis* (African frog) tadpole, a common developmental biology animal model and one used routinely for demonstrating OCT imaging performance[31]. Imaging along the dorsal surface of the tadpole, details of mesenchymal cells were imaged with a 20mm focal length lens at an axial scan rate of 40 Hz. The image has the same corresponding axial and transverse

resolutions, and therefore the same confocal parameter, as the previous image (fig. 7). Fig. 8 illustrates the original and corrected images.

The original image exhibits a loss of transverse resolution out of the confocal region due to the effect of the Gaussian beam, which spreads the energy of a cellular boundary or feature across several pixels, thus blurring and misrepresenting the cellular structure. By comparing cellular regions outside of the confocal region in the two images (boxed regions in fig. 8(a), and 8(b)), the boundaries of the cell membranes and the nuclei appear more distinct in the deconvolved image (fig. 8(b)).

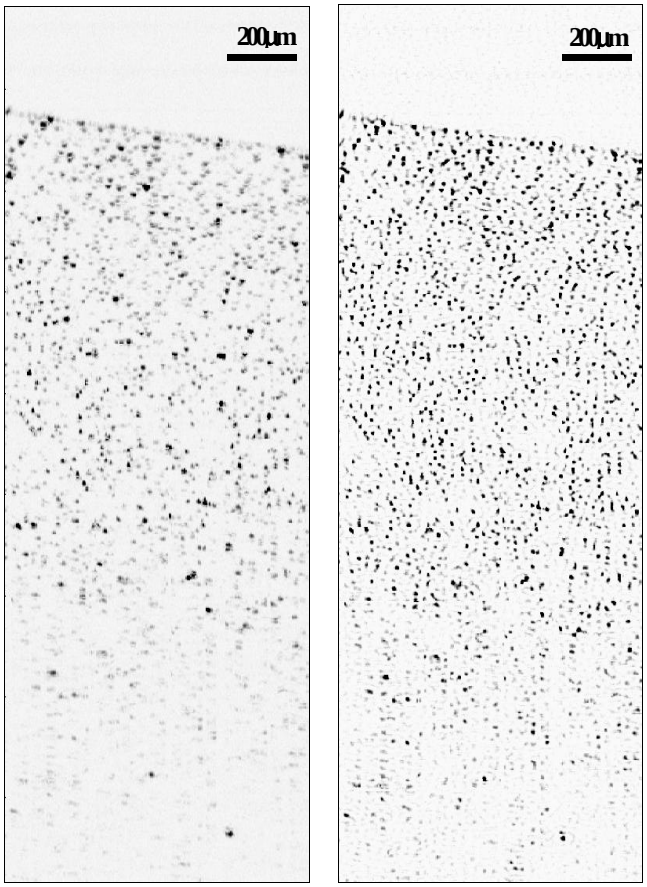

(a) (b)

Fig. 7. Application of the dynamic Richardson-Lucy algorithm on a tissue phantom. (a) Original and (b) Richardson-Lucy corrected image.

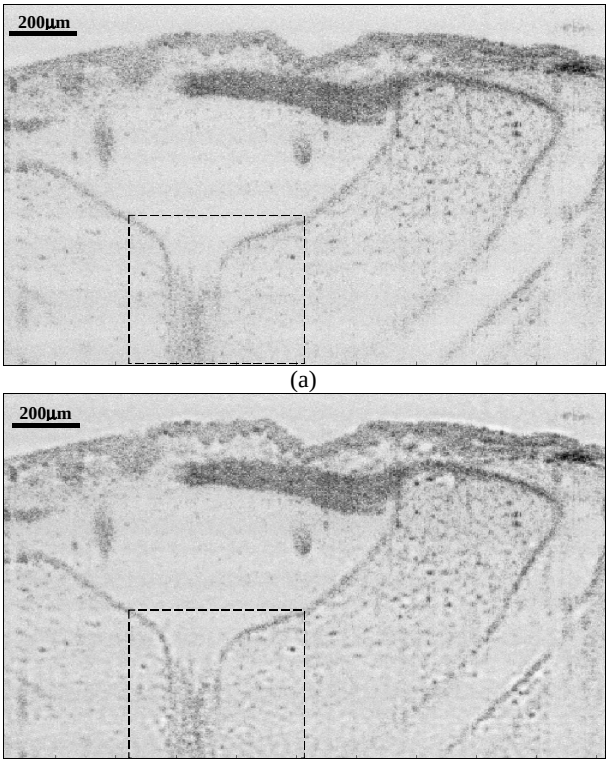

(a)

(b)

Fig. 8. Application of the dynamic Richardson-Lucy algorithm to in vivo cellular data. OCT images of the mesenchymal cells of the Xenopus laevis, represented (a) without deconvolution, and (b) with the dynamic Richardson-Lucy algorithm. Comparison of cellular feature within the dashed box outside the confocal region shows more distinct cell boundaries and features in (b).

CONCLUSIONS

The Richardson-Lucy algorithm tends to concentrate energies near boundaries, which provides a good approximation to cellular boundaries and sub-cellular features, and tends to be more robust against errors from the defocused blur. The Richardson-Lucy algorithm deblurs the intensity of an image therefore concentrating the power near the strong scatterers. These strong scatterers often correspond to the cell nuclei and membranes. Therefore, the implementation of a dynamically-iterative Richardson-Lucy algorithm offers the best performance for distinguishing physical features of the specimen at the cellular level. In particular, the transverse deblurring effect of this algorithm can extend the apparent confocal region of the image, providing high transverse resolution over extended distances, without the need for implementing new optical hardware or the acquisition, segmentation, and assembly of multiple OCT images from the same specimen. The improvements afforded by a dynamically applied Richardson-Lucy algorithm are most pronounced when imaging specimens at the cellular level and at the resolution limits afforded by current OCT systems.

ACKNOWLEDGMENTS

The authors thank Amy Oldenburg, Ron Stack, and Wei Luo from the Beckman Institute for Advanced Science and Technology for their technical contributions to this research, as well as Chenyang Xu for careful review of this manuscript. The animals used in this research were handled and cared for under the approved protocols of the Institutional Animal Care and Use Committee at the University of Illinois Urbana-Champaign.

REFERENCES

1. D. Huang, E. A. Swanson, C. P. Lin, J. S. Schuman, W. G. Stinson, W. Chang, M. R. Hee, T. Flotte, K. Gregory, C. A. Puliafito, and J. G. Fujimoto, "Optical coherence tomography," *Science*, vol. 254, pp. 1178-1181, 1991.
2. J. M. Schmitt, "Optical Coherence Tomography (OCT): A Review," *IEEE Journal of Selected Topics in Quantum Electronics*, vol. 5, pp. 1205-1215, 1999.
3. B. E. Bouma and J. G. Tearney, "The Handbook of Optical Coherence Tomography." New York: Marcel Dekker, Inc., 2001.
4. Z. Chen, Y. Zhao, S. M. Srinivas, J. S. Nelson, N. Prakash, and R. D. Frostig, "Optical Doppler tomography," *IEEE Journal of Selected Topics in Quantum Electronics*, vol. 5, pp. 1134-1141, 1999.
5. A. V. Zvyagin, J. B. Fitzgerald, K. K. M. B. D. Silva, and D. D. Sampson, "Real-time detection for Doppler optical coherence tomography," *Optics Letters*, vol. 25, pp. 1645-1647, 2000.
6. Y. Zhao, Z. Chen, C. Saxer, S. Xiang, J. F. de Boer, and J. S. Nelson, "Phase-resolved optical coherence tomography and optical Doppler tomography for imaging blood flow in human skin with fast scanning speed and high velocity sensitivity," *Optics Letters*, vol. 25, pp. 114-116, 2000.
7. L. B. Lucy, "An iterative technique for rectification of observed distributions," *The Astronomical Journal*, vol. 79, pp. 745-765, 1974.
8. W. H. Richardson, "Bayesian-based iterative method of image restoration," *Journal of the Optical Society of America*, vol. 62, pp. 55-59, 1972.
9. J. A. Izatt, M. R. Hee, G. M. Owen, E. A. Swanson, and J. G. Fujimoto, "Optical coherence microscopy in scattering media," *Optics Letters*, vol. 19, pp. 590-592, 1994.
10. J. L. Starck and E. Pantin, "Deconvolution in Astronomy: A Review," *Publications of the Astronomical Society of the Pacific*, pp. 1051-1069, 2002.
11. P. Shaw, "Deconvolution in 3-D optical microscopy," *Histochem Journal*, vol. 26, pp. 687-694, 1994.
12. M. D. Kulkarni, C. W. Thomas, and J. A. Izatt, "Image enhancement in optical coherence tomography using deconvolution," *Electronics Letters*, vol. 33, pp. 1365-1367, 1997.
13. D. L. Marks, A. L. Oldenburg, J. J. Reynolds, and S. A. Boppart, "Digital algorithm for dispersion correction in optical coherence tomography for homogeneous and stratified media," *Applied Optics*, vol. 42, pp. 204-217, 2003.
14. T. Blu, H. Bay, and M. Unser, "A new high-resolution processing method for the deconvolution of optical coherence tomography signals," presented at IEEE International Symposium on Biomedical Imaging, Washington, DC, USA, 2002.
15. B. Hermann, E. J. Fernandez, A. Unterhuber, H. Sattmann, A. F. Fercher, W. Drexler, P. M. Prieto, and P. Artal, "Adaptive-optics ultrahigh-resolution optical coherence tomography," *Optics Letters*, vol. 29, pp. 2142-2144, 2004.
16. Z. Ding, H. Ren, Y. Zhao, J. S. Nelson, and Z. Chen, "High-resolution optical coherence tomography over a large depth range with an axicon lens," *Optics Letters*, vol. 27, pp. 243-245, 2002.
17. Y. Wang, Y. Zhao, J. S. Nelson, and Z. Chen, "Ultrahigh-resolution optical coherence tomography by broadband continuum generation from a photonic crystal fiber," *Optics Letters*, vol. 28, pp. 182-184, 2003.
18. W. Drexler, U. Morgner, F. X. Kartner, C. Pitris, S. A. Boppart, X. D. Li, E. P. Ippen, and J. G. Fujimoto, "In vivo ultrahigh-resolution optical coherence tomography," *Optics Letters*, vol. 24, pp. 1221-1223, 1999.
19. M. E. Brezinski, G. J. Tearney, S. A. Boppart, E. A. Swanson, J. F. Southern, and J. G. Fujimoto, "Optical biopsy with optical coherence tomography: feasibility for surgical diagnostics," *Journal of Surgical Research*, vol. 71, pp. 32-40, 1997.
20. S. A. Boppart, W. Luo, D. L. Marks, and K. W. Singletary, "Optical coherence tomography: feasibility for basic research and image-guided surgery of breast cancer," *Breast Cancer Research and Treatment*, vol. 84, pp. 85-97, 2004.

21. L. K. Jensen, L. Thrane, P. E. Andersen, A. Tycho, F. Pedersen, S. Andersson-Engels, N. Bendsoe, S. Svanberg, and K. Svanberg, "Optical coherence tomography in clinical examinations of nonpigmented skin malignancies," *Optical Coherence Tomography and Coherence Techniques, Proceedings of the SPIE*, vol. 5140, pp. 160-167, 2003.
22. B. E. A. Saleh and M. C. Teich, *Fundamentals of Photonics*. New York: Wiley, 1991.
23. R. E. Blahut, *Theory of Remote Image Formation*. New York: Cambridge University Press, 2004.
24. Y. Bresler, S. Basu, and C. Couvreur, "Hilbert Spaces and Least Squares Methods for Signal Processing," 2001.
25. D. P. O'Leary, "Near-optimal parameters for Tikhonov and other regularization methods," *SIAM Journal on Scientific Computing*, vol. 23, pp. 1161-1171, 2001.
26. C. R. Vogel, *Computational Methods for Inverse Problems*. New York: SIAM, 2002.
27. L. A. Shepp and Y. Vardi, "Maximum likelihood reconstruction for emission tomography," *IEEE Transactions on Medical Imaging*, vol. 1, pp. 113-122, 1982.
28. P. C. Hansent, "Numerical tools for analysis and solution of Fredholm integral equations of the first kind," *Inverse Problems*, vol. 8, pp. 849-872, 1992.
29. I. Csiszar, "Why least squares and maximum entropy?," *The Annals of Statistics*, vol. 19, pp. 2032-2066, 1991.
30. W. Tan, A. Sendemir-Urkmez, L. J. Fahrner, R. Jamison, D. Leckband, and S. A. Boppart, "Structural and functional optical imaging of three-dimensional engineered tissue development," *Tissue Engineering*, vol. 10, 2004.
31. S. A. Boppart, B. E. Bouma, C. Pitris, G. J. Tearney, J. F. Southern, M. E. Brezinski, and J. G. Fujimoto, "*In vivo* cellular optical coherence tomography imaging," *Nature Med*, vol. 4, pp. 861-864, 1998.